Modeling carbon dioxide transport in PDMS-based microfluidic cell culture devices

A.-J. Mäki[1]*, M. Peltokangas[1], J. Kreutzer[1], S. Auvinen[2], P. Kallio[1]

[1]*Tampere University of Technology, Department of Automation Science and Engineering, BioMediTech, Tampere, Finland*

[2]*Tampere University of Technology, Department of Materials Science, Tampere, Finland*

Abstract

Maintaining a proper pH level is crucial for successful cell culturing. Mammalian cells are commonly cultured in incubators, where the cell culture medium is saturated with a mixture of air and 5% carbon dioxide (CO_2). Therefore, to keep cell culture medium pH in an acceptable level outside these incubators, a suitable CO_2 concentration must be dissolved in the medium. However, it can be very difficult to control and measure precisely local concentration levels. Furthermore, possible undesired concentration gradients generated during long-term cell culturing are almost impossible to detect. Therefore, we have developed a computational model to estimate CO_2 transport in silicone-based microfluidic devices. An extensive set of experiments was used to validate the finite element model. The model parameters were obtained using suitable measurement set-ups and the model was validated using a fully functional cell cultivation device. The predictions obtained by the simulations show very good responses to experiments. It is shown in this paper how the model helps to understand the dynamics of CO_2 transport in silicone-based cell culturing devices possessing different geometries, thus providing cost-effective means for studying different device designs under a variety of experimental conditions without the need of actual testing. Finally, based on the results from the computational model, an alternative strategy for feeding CO_2 is proposed to accelerate the system performance such that a faster and more uniform CO_2 concentration response is achieved in the area of interest.

Keywords: Carbon dioxide; Microfluidics cell culturing; Finite element method; Mass transport; Numerical simulation; pH

*Corresponding author. Tel.: +358 40 7364613
E-mail address: antti-juhana.maki@tut.fi

1. Introduction

In recent years, cell culturing in microscale environments has become an interesting alternative to more conventional macroscale bioreactors. For example, microfluidic-based cell culture devices do not only require smaller volumes of culture medium, but also enable more precise control of the cellular microenvironments. (Kim et al., 2007) In these microfluidic culture devices, poly(dimethylsiloxane) (PDMS) has become the most popular material because of its simple fabrication process, low cost, optical transparency, biocompatibility and gas permeability. (Duffy et al., 1998; Gao et al., 2012) Using gas permeability properties, several PDMS-based microfluidic devices have been developed to generate desired oxygen (Adler et al., 2010; Chen et al., 2011; Inamdar et al., 2011; Polinkovsky et al., 2009; Shiku et al., 2006; Skolimowski et al., 2010; Zahorodny-Burke et al., 2011) and carbon dioxide (CO_2) (Forry and Locascio, 2011; Polinkovsky et al., 2009; Takano et al., 2012) concentrations for cell cultures.

CO_2 is typically used for controlling pH in the cell culture medium (Kim et al., 2007), and therefore it is a crucial parameter especially in long-term cell culture studies outside an incubator. There are several methods to supply the required CO_2 concentration to the medium in the microfluidic cell culture devices. For example, gas permeability of PDMS allows that CO_2 can be fed to the culture medium through a PDMS-membrane instead of feeding CO_2 directly to liquid, reducing a liquid loss by evaporation and further stabilizing osmolarity. (Blau et al., 2009)

While oxygen transport in PDMS-based microfluidic cell culture devices has been modeled in various studies (Adler et al., 2010; Chen et al., 2011; Inamdar et al., 2011; Polinkovsky et al., 2009; Shiku et al., 2006; Skolimowski et al., 2010; Zahorodny-Burke et al., 2011), CO_2 transport has not been comprehensively modeled. Therefore, we have developed a computational CO_2 transportation model that is based on a finite element method (FEM). The model provides a tool for designing PDMS based cell culture systems and for studying CO_2 concentration levels especially when concentration measurement is impossible or difficult.

The rest of the paper is organized as follows: first, theory required for the model is explained before presenting measurements used to validate the computational model developed in this paper. This model is presented next before comparing experimental values and results from simulations. Finally, the verified model is used for studying CO_2 transport in different devices.

2. Theory

Required equations for the numerical are described in this section. First, CO_2 transport modeling is covered before presenting equations required for estimation of liquid pH in cell culturing devices.

2.1. Carbon dioxide transport and concentration

In a PDMS cell culture device, CO_2 concentration can be in gas, liquid and solid phases (Forry and Locascio, 2011; Polinkovsky et al., 2009). In this study, the solid phase refers to the CO_2 concentration within the PDMS parts (shown as grey areas in Fig. 2B). Therefore, to model the entire system, CO_2 transport mechanisms in these three phases need to be described. In the fluidic phases (gas and liquid), CO_2 is transported by both diffusion and convection. In the solid phase there is no convection; the transport is diffusion-driven, as CO_2 diffuses through material due to concentration differences across material. When assuming no material consumption, three different mass transport equations describes a mass balance in the system (Stoian et al., 2012):

$$\begin{aligned}
&\frac{\partial c_g}{\partial t} + \nabla \cdot \left(-D_g \nabla c_g\right) + \boldsymbol{u_g} \cdot \nabla c_g = 0 \\
&\frac{\partial c_l}{\partial t} + \nabla \cdot \left(-D_l \nabla c_l\right) + \boldsymbol{u_l} \cdot \nabla c_l = 0 \\
&\frac{\partial c_p}{\partial t} + \nabla \cdot \left(-D_p \nabla c_p\right) = 0
\end{aligned} \qquad (1)$$

where subscripts g, l, and p denote the CO_2 concentration in gas-phase, liquid-phase, and solid-phase (PDMS), and c, D, and $\boldsymbol{u}$ are CO_2 concentration, diffusion coefficient, and velocity field, respectively, in each phase. Equation (2) describes equilibrium of CO_2 concentration between i) liquid and gas, ii) liquid and PDMS, and iii) PDMS and gas (Shiku et al., 2006; Skolimowski et al., 2010):

$$c_l \underset{k_{gl}}{\overset{k_{lg}}{\rightleftharpoons}} c_g, c_l \underset{k_{pl}}{\overset{k_{lp}}{\rightleftharpoons}} c_p, c_p \underset{k_{gp}}{\overset{k_{pg}}{\rightleftharpoons}} c_g \qquad (2)$$

where k represents the mass transport coefficient at the specific surface, and subscript indicates the direction; e.g. k_{lp} provides the mass transport coefficient from the liquid-phase to the PDMS-phase at the interfaces between these two phases. A dimensionless partition coefficient ratio between two domains, Kp, is calculated using the saturated concentration values (Shiku et al., 2006; Skolimowski et al., 2010):

$$\begin{aligned}
Kp_{lg} &= \frac{k_{lg}}{k_{gl}} = \frac{c_{g_sat}}{c_{l_sat}} \\
Kp_{lp} &= \frac{k_{lp}}{k_{pl}} = \frac{c_{p_sat}}{c_{l_sat}} \\
Kp_{pg} &= \frac{k_{pg}}{k_{gp}} = \frac{c_{g_sat}}{c_{p_sat}}
\end{aligned} \qquad (3)$$

where c_{g_sat}, c_{l_sat}, and c_{p_sat} are saturated CO_2 concentrations in gas, liquid, and PDMS domains, respectively. Based on the previous equations, mass transport at the interfaces between two different domains is modeled using mass transport coefficients and CO_2 concentrations in both sides of the interfaces. These fluxes between two phases are modeled using the following equations (separately for each interface; liquid/gas, liquid/PDMS, and PDMS/gas) (Shiku et al., 2006; Skolimowski et al., 2010):

$$Flux_{lg} = k_{lg}c_l - k_{gl}c_p = k_{gl}\left(Kp_{lg}c_l - c_g\right)$$
$$Flux_{lp} = k_{lp}c_l - k_{pl}c_g = k_{pl}\left(Kp_{lp}c_l - c_p\right) \quad (4)$$
$$Flux_{pg} = k_{pg}c_p - k_{gp}c_g = k_{gp}\left(Kp_{pg}c_p - c_g\right)$$

where $Flux_{lg}$, $Flux_{lp}$, and $Flux_{pg}$ denote the CO_2 flux towards the gas-phase at the liquid/gas interface, the flux towards the PDMS-phase at the liquid/PDMS interface, and the flux towards the gas-phase at the PDMS/gas interface, respectively. Negative sign is used for the opposite flux direction.

As the saturated concentrations in each domain are used for defining value of Kp, these are determined next. In the gas phase, the saturated CO_2 concentration is estimated by assuming that the ideal gas law is valid, and is therefore calculated using an equation:

$$p_{CO2}V = nRT, c_{g\_sat} = \frac{n}{V}$$
$$\Rightarrow c_{g\_sat} = \frac{p_{CO2}}{RT} = \frac{Fv_{CO2}p_{ch}}{RT} \quad (5)$$

where p_{CO2}, V, n, R, T, Fv_{CO2}, and p_{ch} are CO_2 partial pressure, volume, amount of substance, the ideal gas constant, temperature, volume fraction of CO_2 gas component, and total pressure in the chamber, respectively.

If CO_2 is assumed as an ideal gas, Henry's law that describes the equilibrium between vapor and liquid defines CO_2 concentration in the liquid phase. Henry's law as a function of temperature can be then used to calculate dissolved CO_2 concentration in liquid (Sander, 1999):

$$kh_{H(T)} = kh_{H0}exp\left[-H\left(\frac{1}{T} - \frac{1}{T_{SATP}}\right)\right]$$
$$c_{l\_sat(T)} = \frac{p_{CO2}}{k_{H(T)}} \quad (6)$$

where $kh_{H(T)}$, kh_{H0}, T_{SATP}, H, and $c_{l\_sat(T)}$ are Henry's law constant at experiment temperature T, Henry's law constant at standard ambient temperature T_{SATP} (298.15 K), a constant used to calculate temperature dependent Henry's law constant (in K) and saturated CO_2 concentration in liquid at experiment temperature T, respectively.

Finally, the saturated CO_2 concentration in PDMS is calculated based on the solubility of CO_2 in PDMS (Merkel et al., 2000):

$$S = Sinf(1 + p_{ch}np)$$
$$c_{p\_sat} = Sc_{g\_sat} \quad (7)$$

where *S*, *Sinf*, and *np* are the solubility of CO_2 in PDMS, the infinite dilution solubility, and the pressure dependence of solubility, respectively. When solubility and permeability properties are known, diffusion coefficient of CO_2 in PDMS, D_p, is estimated using equation (Charati and Stern, 1998):

$$D_p = \frac{P}{S} \quad (8)$$

where *P* is the permeability coefficient of CO_2 in PDMS. Using this equation, the mean diffusion coefficient is solved when solubility is known and the permeability coefficient is determined with experiments explained in Section 3.1.

2.2. Carbonate reaction

In the pH measurement, reaction between CO_2 and liquid (water) when CO_2 is dissolved in liquid should be considered. The overall carbonate reaction in solution (water) is following (Forry and Locascio, 2011):

$$CO_{2(gas)} \Leftrightarrow CO_{2(aq)}$$
$$CO_{2(aq)} + H_2O \Leftrightarrow H_2CO_3 \Leftrightarrow H^+ + HCO_3^- \quad (9)$$
$$HCO_3^- \Leftrightarrow H^+ + CO_3^{2-}$$

where $[CO_{2(aq)}]$, $[H_2CO_3]$, $[HCO_3^-]$, $[H^+]$, and $[CO_3^{2-}]$, are the concentrations of the dissolved CO_2 in liquid, carbonic acid, bicarbonate ion, hydrogen ion, and carbonate ion, respectively. In this study, $[CO_{2(aq)}]$ equals c_l in Eq. (2). As the hydration equilibrium constant *Khyd*, $[H_2CO_3]/[CO_{2(aq)}]$ is around 1.7×10^{-3} (Forry and Locascio, 2011), less than 0.2 percent of $CO_{2(aq)}$ molecules are converted to $[H_2CO_3]$, thus majority of the dissolved CO_2 exists as $CO_{2(aq)}$. Similarly, as $[CO_3^{2-}]$ is not significant compared to $[HCO_3^-]$ at the pH level used in this study (smaller than 7), it will not be included in the analysis (Liu et al., 2012). Using these assumptions, liquid pH can be approximated very precisely in the experimental conditions using the following equation:

$$pH = -log_{10}([H^+]) \approx -log_{10}\left(\sqrt{Kw + c_lKc}\right) \quad (10)$$

where *Kw* and *Kc* are the ion product of water ($\sim10^{-14}$ at room temperature) and the thermodynamic constant for the dissociation of $[H_2CO_3]$, respectively. The latter can be approximated at a certain temperature *T* between 0 to 50°C (converted to Kelvin) using constants *A*, *B*, and *C* in equation (Millero and Pierrot, 1998):

$$Kc = exp\left(A + \frac{B}{T} - C\,ln(T)\right) \quad (11)$$

where A = 290.9097, B = -14554.21, C = -45.0575 for [H_2CO_3], and T is unitless in the equation. Using these, Kc is around 4.4×10^{-3} at 24°C.

3. Experimental set-ups

The developed computational model has five unknown parameters, D_l, D_p k_{gl}, k_{gp}, and k_{pl}, which were determined experimentally in this work. To define these unknown parameters, four different measurements were performed. First, permeability coefficient of CO_2 in PDMS was measured with a commercial device, and the results were used to define the range of diffusion coefficient D_p using Eq. (8). Next, two measurement set-ups including a CO_2 gas sensor were used to determine the needed simulation parameters. It was also possible to obtain the dynamics of CO_2 transport using these measurements. Finally, pH measurement was performed to validate the developed model in the complete device.

3.1. CO_2 measurements for the model development

Three types of phase-interfaces exist in PDMS-based cell culture devices: gas-liquid, gas-solid, and liquid-solid as explained in Section 2.1. Measurements required obtaining the model parameters for each phase-interfaces and domains are described next. First, permeability of CO_2 in PDMS was measured using a carbon dioxide transmission rate testing system PERMATRAN-C Model 4/41 (MOCON, Inc., USA). In these experiments, a gas mixture containing 5% of CO_2 and 95% of N_2 (AGA, Finland) was used to measure the CO_2 transmission rate in ten different PDMS samples. The samples had a measurement area of 5 cm^2 and thicknesses between 1.72 mm and 2.92 mm. Temperature and pressure difference between sample sides were maintained at 23°C and 1 atm (vacuum), respectively, during the experiments. The measured transmission rates (unit: $cm^3\cdot(m^2\cdot day\cdot atm)^{-1}$) were multiplied with measured sample thicknesses (unit: mm), and then the received value (unit: $(cm^3\cdot mm\cdot (m^2\cdot day\cdot atm)^{-1}$) was converted to Barrers (1 Barrer = 65.664 $cm^3\cdot mm\cdot(m^2\cdot day\cdot atm)^{-1}$ (McKeen, 2012)). Next, two sets of measurements, *M1* and *M2*, were performed to define the required model parameters: six measurements with a gas-PDMS-gas interface (*M1a*…*M1f*) to determine D_p, and k_{gp}, and five measurements with a gas-liquid-PDMS-gas interface (*M2a*…*M2e*) to determine D_l, k_{gl}, and k_{pl}.

The PDMS sheets were fabricated by mixing PDMS prepolymer and curing agent (Sylgard 184, Dow Corning, USA) in a standard 10:1 ratio, poured into a 55-mm diameter Petri dish, de-gassed in a vacuum, and cured at 60°C for three hours. After fabrication, the sheets were stored in a closed Petri-dish in normal room temperature and humidity

maximum ten days before placed in the measurement system. The system consisted of two chambers separated by a PDMS sheet on a 5-mm-thick gas impermeable glass plate having a hole of 20 mm in a diameter as shown in Fig. 1. A gas mixture containing CO_2 was supplied to the upper chamber made from polypropylene), whereas a CO_2 sensor was placed inside the initially CO_2-free lower chamber. The upper chamber has a cylinder shape with a volume of 0.7 l, a diameter of 112 mm and a height of 72 mm. The lower chamber has a volume of 0.25 l with an outer height of 56 mm, an outer length of 72 mm and an outer width of 70 mm. The PDMS sheet on the glass plate covered the 20 mm hole and the glass plate entirely. In the gas-PDMS-gas measurements, no other parts were used, whereas in the gas-liquid-PDMS-gas measurements, an additional 5-mm-thick glass plate having a hole with a diameter of 20 mm was first placed on the PDMS sheet and then the pool formed was filled with de-ionized water (Fig. 1).

The measurement range of the used non-dispersive CO_2 sensor based on infrared detection (COZIR Wide Range GC-0006, CO2Meter, USA, accuracy ± 5% of reading) was 0%-20% and it was calibrated by using a gas mixture containing 5% of CO_2, 19% of O_2 and 76% of N_2 (AGA, Finland). The diameter of the active area of the sensor was 20 mm, and therefore, the sensor was tightly fixed to the hole of the glass plate. In order to prevent the pressure increase in the lower chamber while gassing the upper chamber, a small hole (diameter 0.5 mm) was drilled close to the bottom of the lower chamber (Fig. 1).

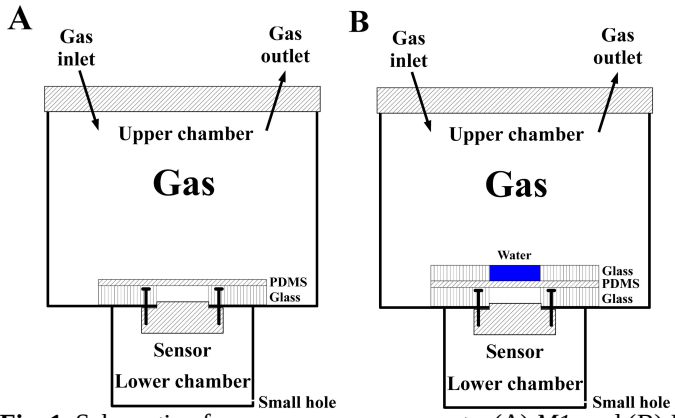

Fig. 1. Schematic of gas sensor measurements: (A) *M1*, and (B) *M2*.

Three different PDMS thicknesses (2000±10 µm, 380±10 µm and 110±10 µm, measured using a digital caliper before the experiments) and two different gas mixtures, 5% CO_2 and 100% CO_2, were used in the experiments. The gauge pressure of the gas mixture varied between 17 mbar and 36 mbar. Temperature was monitored during the experiments and was always between 22.8°C and 24°C. Detailed information on each experiment is shown in Table 1 including the average experimental temperature in every measurement.

Table 1
Experimental conditions in measurements *M1* and *M2*.

	Measurement set 1						Measurement set 2				
Parameter	***M1a***	***M1b***	***M1c***	***M1d***	***M1e***	***M1f***	***M2a***	***M2b***	***M2c***	***M2d***	***M2e***
Average temperature (°C)	23	23	24	24	24	24	23	24	24	24	24
Gauge pressure (mbar)	28	28	17	17	17	19	36	34	18	18	24
Feeding CO_2 (%)	100	100	100	5	5	5	5	5	5	5	5
PDMS thickness (µm)	2000	2000	110	110	110	380	110	110	380	380	380

Before each measurement, the chambers were aired in order to remove the CO_2 residues from the chambers. This was done by removing the PDMS sheet between the chambers and keeping the upper measurement chamber open. The measurement chamber was kept open for at least as long as the CO_2 sensor output agreed with the background CO_2 level. After the ventilation, the PDMS sheet was tightly placed on the glass plate. In the case of the gas-liquid-PDMS-gas experiment, the additional glass plate was placed on the PDMS sheet and the pool was filled with water as described earlier. Next, the upper chamber was closed, the gas inlet and the gas outlet were connected and recording of the CO_2 concentration was started with a sampling frequency of 1 Hz. Finally, the pressure regulators for the gas lines were opened and the gauge pressure was logged using a pressure sensor (HCXM050D6V, First Sensor AG, Germany) connected into the gas inlet. The measurement was continued until the sensor output was stabilized to 5% level (measurements with 5% CO_2) or reached the measurement range of the sensor (measurements with 100% CO_2).

Two first measurements using a 2000-µm-thick PDMS layer (labeled as *M1a* and *M1b*) were used for determining k_{gp} and the diffusion coefficient of CO_2 in PDMS, D_p. The rest of the measurements (*M1c*… *M1f* and *M2a*… *M2e*) were performed to obtain remaining parameters (D_l, k_{gl}, and k_{pl}) required for the developed CO_2 transport model.

3.2. pH measurement

A complete structure, designed for cell culture purposes (Fig. 2), was used for the validation of the proposed model. The structure consists of two parts: a culture well and a connection cap. The culture well was fabricated from a 6-mm-high PDMS ring by punching a 12 mm hole in the middle. The connection cap consists of four layers: a 6-mm-thick PDMS layer on top for tight and sealed connections for gas supply pipes, a 1 mm glass layer providing rigidity, a 3-mm-thick PDMS layer below the glass, and a 500-µm-thick PDMS membrane. The membrane seals the culture well water-tightly, but lets the gas pass through. All PDMS parts were fabricated with same process that was described in Section 3.1.

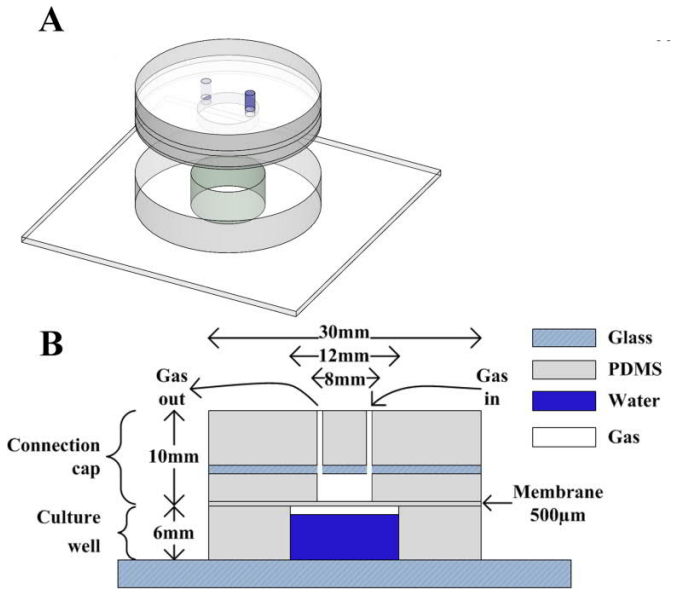

Fig. 2. The schematic of the cell cultivation device: (A) 3D view and (B) the cross-sectional view.

The pH validation experiments were performed in typical room conditions (temperature, humidity). The culture well was filled with de-ionized water (volume 600 µl). The connection cap was placed on top of the culture well and dry gas mixture (5% CO_2) was supplied from the inlet port as shown in Fig. 2B. In these experiments, a gas flow rate of 1 ml/min was used. In a selected time interval, pH was measured by removing the connection cap and taking a 200 µl sample to a pipette tip. The sample was taken at the bottom of the culture well to obtain a pH value representative at the cell cultivation area. The pH was measured inside the pipette tip using a small field-effect transistor (FET) type pH probe (MicroFET, Sentron Europe BV, The Netherlands) that includes an integrated temperature sensor. The experimental conditions were following: an average temperature 23.7°C and a chamber pressure 1 atm. Each measurement was recorded for two minutes continuously, and an average pH and a standard deviation (SD) were calculated. Recordings were conducted in several time-points (0, 10, 25, 40, 60, and 75 min). Additionally, four long-term measurements (two one day and two five days) were performed to determine the equilibrium pH value of the device.

4. Computational model

In this section, the developed computational model is presented. Model properties are described before reporting the implementation of the model using commercial software. As mentioned in Section 3, the developed computational model had five unknown parameters (D_l, D_p, k_{gl}, k_{gp}, and k_{pl}) which were determined experimentally.

4.1. Model parameters, assumptions, geometry, and boundary conditions

This section describes the model parameters, assumptions, geometries, and boundary conditions used for simulating CO_2 concentrations in the PDMS device. Mass transport between different phases is based on the flux in the boundaries as explained in Section 2.1. Several assumptions and simplifications were included in the model. Firstly, it assumes that both the ideal gas behavior and the Henry's Law are valid. Also, constant temperature and pressure conditions are used in the model. Furthermore, liquid evaporation and possible leaking are expected to be negligible. Dissolution and transportation of other molecules (for instance oxygen from air) are not considered in the model. Because only a very small amount of dissolved CO_2 concentration (c_l) converts to [HCO_3^-], as discussed in Section 2.1, and c_l is the main carbonate specie in the aqueous phase; c_l is not consumed and thus, reactions between CO_2 and liquid (water) are ignored in the model. As no perfusion is included, fluid (liquid and gas) velocities ($\boldsymbol{u}$ in Eq. (1)) are set to zero.

Two-dimensional axial-symmetric models for the parameter determination measurements sets (M_1 and M_2) presented in Section 3.1 were created as shown in Fig. 3. The dimensions in the models were the following (see also Section 3.1 and Fig. 1): an outer radius 27.5 mm, an inner gas chamber radius and a height: 10 mm and 4.9 mm, respectively, and a width and a height of the glass plate: 17.5 mm and 6 mm. Feeding CO_2 values (%) from Table 1, converted to concentration values using the ideal gas law, were set on the top boundary in both models. The left boundary was defined as the symmetry line and no flux condition was set on the sensor surface and the glass boundaries. The initial concentrations are based on the saturated concentrations in each phase (gas, liquid, solid) when exposed to air, where CO_2 concentration is approximately 0.04%.

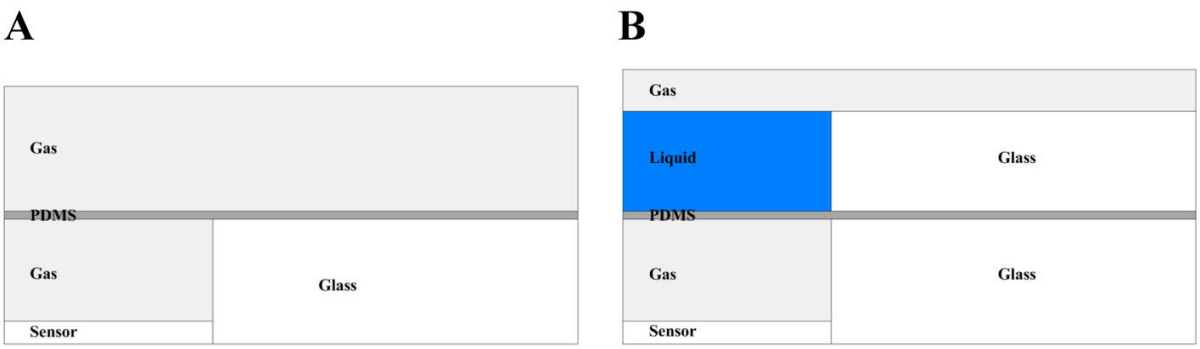

Fig. 3. Geometries used for parameter determination experiments: (A) *M1*, and (B) *M2*. Axial symmetry is set to left boundary on both models.

Compared to the experimental set-up used in pH measurement reported in Section 3.2, a simplified version concerning only the part below the glass plate (an outer radius 15 mm, a total height 9.5 mm, shown in Fig. 2) was used. In the simplified model, 500 µm space above the PDMS membrane was analysed, resulting in a total height of 7 mm as shown in Fig. 4. Because of the symmetry of the device, two-dimensional axial-symmetric model was also used in this case. The left boundary was defined as the symmetry line and no flux condition was set on the bottom surface of the device and the glass boundaries in the top part. Revolution of this model is shown in Fig. 4. 5% CO_2 concentration was set to the top gas layer in the middle of the device as showing in Fig. 4.

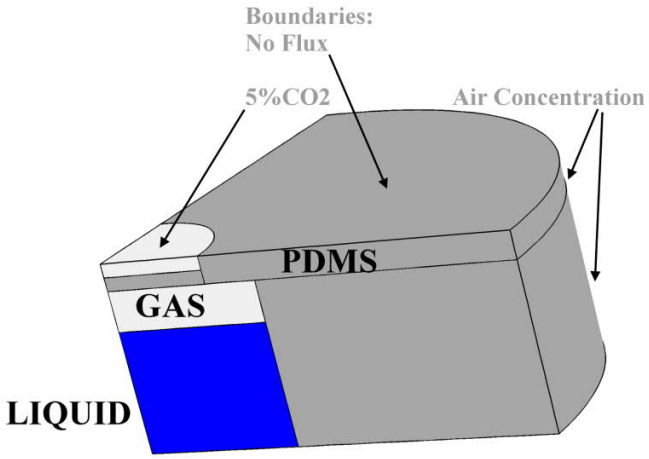

Fig. 4. pH model geometry, phases and boundaries. No flux condition was set also to the bottom boundaries (not shown).

In every model, CO_2 transport between two phases is based on the flux given in Eq. (4) using *Kp*, the partition coefficient ratio between two domains. *Kp* is calculated based on the saturated concentrations using Eq. (5), (6), and (7) for gas, liquid, and solid (PDMS) phases, respectively, and for each experiment conditions separately.

4.2. Model implementation

Time-dependent carbon dioxide concentrations were solved using a commercial finite-element modeling tool COMSOL Multiphysics® Version 4.4 (COMSOL, Inc., USA). In the models, "Transport of diluted species equations" using Fick's law was used as the governing equation to calculate the time-dependent CO_2 concentration profile. The used computational meshes for the models were following; for measurement set *M1*, the mesh consisted of ~3100 triangular elements for simulations of 380-µm-thick and 2000-µm-thick PDMS membranes, and ~7100 triangular elements for simulations of 110-µm-thick PDMS membranes. In the measurement set *M2*, ~3300 and ~7200 triangular

elements were used for simulations of 380-µm-thick and 110-µm-thick PDMS membranes, respectively, whereas the model used for both pH measurement and simulation case study (presented in Section 5.3) consisted of ~3600 triangular elements. All the simulations were carried out using Intel i7-960 3.2GHz processor with 24 GB of memory using direct PARDISO solver.

5. Results and Discussion

This section describes first the determination of the parameters for the computational model using experiments explained in Section 3.1. Then, results from the model are compared to pH measurement presented in Section 3.2. Finally, it is demonstrated how the developed model is used for testing a variety of different experimental conditions to discover the required inlet CO_2 concentration to maintain a desired CO_2 concentration level.

5.1. Determination of the model parameters

The model parameters were determined using the measured carbon dioxide concentrations reported in Section 3. The parameters of the model and their values are listed in Table 2. As described earlier, the model had five unknown parameters, D_l, D_p k_{gl}, k_{gp}, and k_{pl}, which were determined experimentally in this work. The infinite dilution solubility constant at 24°C, *Sinf*, was approximated based on published values around the same temperature (Blau et al., 2009; Shah et al., 1993; Tanimura, 1993). The CO_2 diffusion coefficient in a gas-phase, D_g, was approximated based on literature (Davidson and Trumbore, 1995; Terashima et al., 2001).

The modeling process included over thirty simulation runs to determine the parameter values. First, permeability experiments presented in Section 3.1 were performed to define the diffusion coefficient D_p. The measured permeability coefficient values varied between 8000 and 10 000 Barrers (1 Barrer = 7.6×10^{-9} $cm^3(STP)\cdot cm\cdot(cm^2\cdot s\cdot atm)^{-1}$). Using these values and the solubility S of CO_2 in PDMS given in Table 2, together with Eq. (8), the estimated value for D_p varies between 4.1-5.1×10^{-9} $m^2\cdot s^{-1}$. Next, as described earlier, the model was simulated with different D_p (between 2-6×10^{-9} $m^2\cdot s^{-1}$) and k_{gp} values using six different experimental conditions *M1* given in Table 1. Measurements *M1a* and *M1b* using the 2-mm-thick PDMS membranes were used to define a more precise value for D_p and k_{gp}. During the model parameter iteration process, it was noticed that D_p must be remarkably higher than typically reported in the literature, around 2-3×10^{-9} $m^2\cdot s^{-1}$ (e.g. Jawalkar and Aminabhavi, 2007). This confirmed, that the D_p values (4.1-5.1×10^{-9} $m^2\cdot s^{-1}$) obtained in the permeability measurements were in the correct range. Next, all six *M1* experiments (*M1a-M1f*) were simulated by varying D_p between 4.1-5.1×10^{-9} $m^2\cdot s^{-1}$, and changing k_{gp} in the model for several orders

of magnitude. Finally, comparing the model results to the experimental data *M1*, a combination of D_p and k_{gp} that gave the best overall response was chosen.

The other model parameters, k_{gl}, k_{pl}, and D_l, were determined using a similar process by comparing the model results to the data set *M2* and using the values chosen for D_p and k_{gp}. First, to detect the lowest possible limit for D_l, measurements *M2a* and *M2b* were simulated so that parameters k_{gl} and k_{pl} were changed in the model for several orders of magnitude. Using this approach, it was noticed that to provide a proper simulation response, D_l must be larger than 20×10^{-9} $m^2 \cdot s^{-1}$, value that is over an order of magnitude higher than expected based on literature, around 2×10^{-9} $m^2 \cdot s^{-1}$ (Sell et al., 2013; Xu et al., 2012). Next, based on literature, k_{gl} was assumed to be in the order of 10^{-5} or 10^{-4} $m \cdot s^{-1}$ (Clark et al., 2011; Han et al., 2013; Ocampo-Torres and Donelan, 1994). Keeping k_{gl} in this range, changing k_{pl} again in several orders of magnitude (between 10^{-7} and 10^{-1} $m \cdot s^{-1}$), and altering D_l between $20\text{-}100\times10^{-9}$ $m^2 \cdot s^{-1}$, the model was simulated with all measurements conditions *M2a-M2e*. It was noticed, that k_{pl} must be in the order of 10^{-5} $m \cdot s^{-1}$. Again, model parameters that gave the best overall response to measurement set *M2* were chosen. Finally, the full model was validated by comparing the simulated results to the data obtained from the pH measurement presented in Section 3.2.

The final step in the model development was to study the confidence bounds of the model parameters. An important issue to consider is the measurement accuracy when determining these parameters. As noted earlier, accuracy of the CO_2 sensor was ±5% of the reading, and the accuracy of the membrane thickness measurement was ±10µm. Therefore, the total measurement confidence is around ±10%. It should be stated that this measurement inaccuracy is also the minimum uncertainty of the model. Next, the sensitivity of the chosen model parameters was analyzed. For D_p, the permeability measurement gave a result of $4.1\text{-}5.1\times10^{-9}$ $m^2 \cdot s^{-1}$. For D_l, k_{gl}, k_{pl}, and k_{gp}, it was noted, that maximum 20% difference is possible for acceptable simulation response, therefore this was chosen as the confidence bound in Table 2.

Table 2
Used simulation parameters.

Parameter	**Value**	**Source**
Temperature, T	23- 24°C	Measured
Gauge pressure in chamber, p	17 - 36 mbar	Measured
Liquid density, ρ	997.5 - 997.3 $kg \cdot m^{-3}$	Water properties
Liquid dynamic viscosity, η	$9.4 - 9.1\times10^{-4}$ $Pa \cdot s$	Water properties
Universal gas constant, R	8.31451 $J \cdot (K \cdot mol)^{-1}$	

Henry's law constant for CO_2 in water at 25°C, k_{H0}	29.41 l·atm·mol^{-1}	(Sander, 1999)
Constant to convert k_H to $k_{H(T)}$, H	2400 K	(Sander, 1999)
$k_{H(T)}$ for CO_2 at T, $k_{H(T)}$	27.9-28.6 l·atm·mol^{-1}	Calculated using Eq. (6) (Sander, 1999)
The pressure dependence of solubility constant of CO_2 in PDMS, n	5.9×10^{-3} atm^{-1}	(Merkel et al., 2000)
Solubility constant of CO_2 in PDMS at chamber pressure and 24°C, S	1.5 cm^3(STP)·cm^{-3}·atm^{-1}	Approximated using Eq. (7) (Merkel et al., 2000)
The infinite dilution solubility constant of CO_2 in PDMS at 24°C, *Sinf*	1.5 cm^3(STP)·cm^{-3}·atm^{-1}	Approximated (Blau et al., 2009; Shah et al., 1993; Tanimura, 1993)
Diffusion coefficient for CO2 in gas, D_g	1.6×10^{-5} m^2·s^{-1}	Approximated (Davidson and Trumbore, 1995; Terashima et al., 2001)
Diffusion coefficient for CO_2 in PDMS, D_p	4.2×10^{-9} m^2·s^{-1}	Determined using permeability and *M1* measurements Range: $4.1\text{-}5.1\times10^{-9}$ m^2·s^{-1}
Diffusion coefficient for CO_2 in liquid, D_l	$(30\pm6)\times10^{-9}$ m^2·s^{-1}	Determined using measurement *M2*
Dissociation constant of H_2CO_3 in water, *Khyd*	1.7×10^{-3}	(Forry and Locascio, 2011)
Mass transport coefficient from the gas-phase to the liquid-phase, k_{gl}	$(6.0\pm1.2)\times10^{-5}$ m·s^{-1}	Determined using measurement *M2*
Mass transport coefficient from the gas-phase to the solid (PDMS)-phase, k_{gp}	$(1.0\pm0.2)\times10^{-5}$ m·s^{-1}	Determined using measurement *M1*
Mass transport coefficient from the liquid-phase to the solid (PDMS)-phase, k_{pl}	$(1.5\pm0.3)\times10^{-5}$ m·s^{-1}	Determined using measurement *M2*
Partition coefficient ratio between, liquid and solid (PDMS) domains, Kp_{lp}	1.77	Approximated using Eq. (3)
Partition coefficient ratio between liquid and gas domains, Kp_{lg}	1.17	Approximated using Eq. (3)
Partition coefficient ratio between solid (PDMS) and gas domains, Kp_{pg}	0.66	Approximated using Eq. (3)
Thermodynamic constant for the dissociation of [H_2CO_3], *Kc*	4.4×10^{-3}	Approximated using Eq. (11) (Millero and Pierrot, 1998)

D_l, D_p, k_{gl}, k_{gp}, and k_{pl} were determined in this work.

Fig. 5 compares the simulated results using parameters chosen for D_p and k_{gp} and the experiments of data set *M1*. As can be seen, the model is able to capture the dynamics of the CO_2 transport and predicts CO_2 concentration remarkably well in six different experiments with different temperatures (between 23°C and 24°C), gauge pressures

(from 17 mbar to 36 mbar), CO_2 feed level (5% and 100%), and PDMS thicknesses (110 µm, 380 µm, and 2 mm). Fig. 6 shows a comparison between data set *M2* and simulation using all the model parameters given in Table 2, and demonstrates that the model predicts accurately the CO_2 transport behavior in the device including liquid-phase.

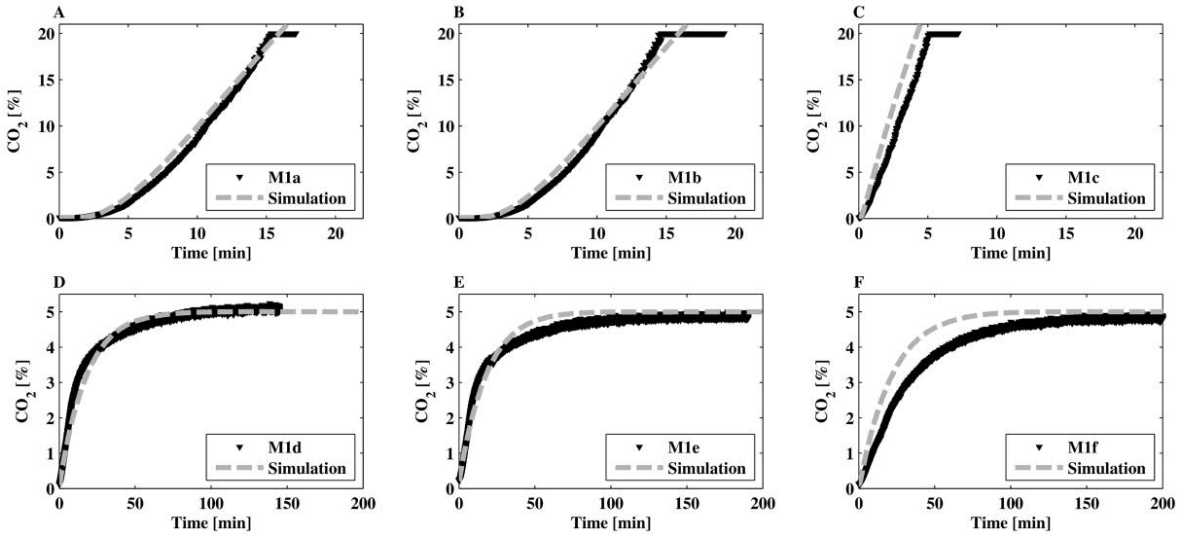

Fig. 5. Determination of model parameters D_p, and k_{gp} using measurement set *M1*: (A) *M1a*, (B) *M1b*, (C) *M1c*, (D) *M1d*, (E) *M1e*, and (F) *M1f*.

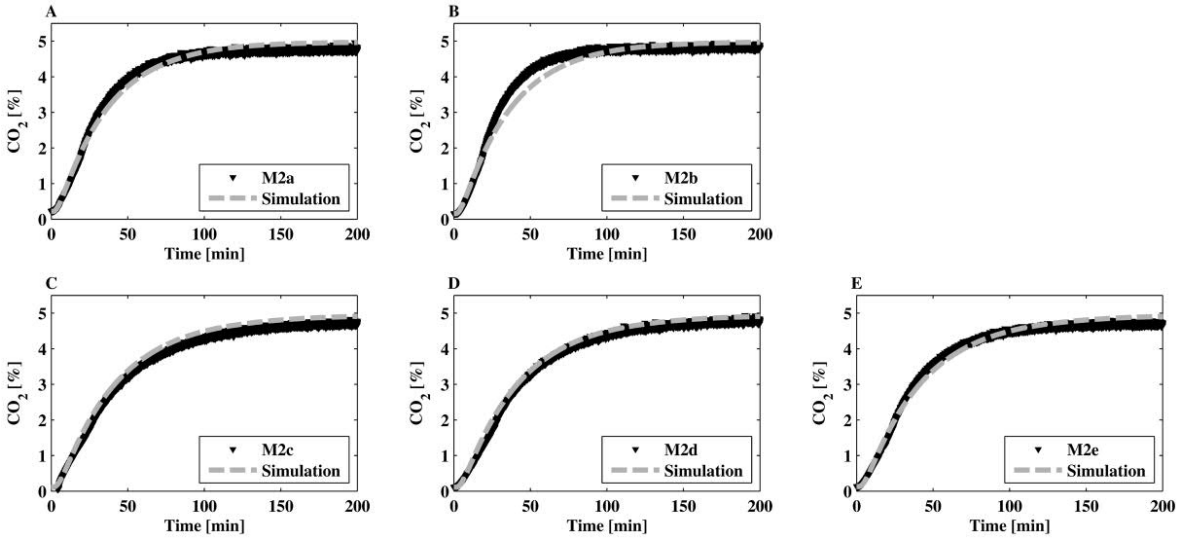

Fig. 6. Determination of the model parameters D_l, k_{gl}, and k_{pl} using measurement set *M2*: (A) *M2a*, (B) *M2b*, (C) *M2c*, (D) *M2d*, and (E) *M2e*.

Some of the determined values require a further discussion. Firstly, value determined for the diffusion coefficient D_p, 4.2×10^{-9} $m^2\cdot s^{-1}$ at around 24°C is larger than values typically given in the literature (around $2.2 - 2.6\times10^{-9}$ $m^2\cdot s^{-1}$). However, as stated earlier, D_p can also be estimated based on permeability coefficient and solubility of CO_2 in PDMS using Eq. (8). As explained earlier, the measured diffusion coefficient D_p based on the permeability experiments, was between $4.1\text{-}5.1\times10^{-9}$ $m^2\cdot s^{-1}$, supporting the selected parameter value. It should also be stated that there are significant differences between values for D_p in the literature; for example Blau *et al*. and Kuo reported D_p values to be within $2.2\text{-}11\times10^{-9}$ $m^2\cdot s^{-1}$ (Blau et al., 2009; Kuo, 1999) at 25°C. On the other hand, D_p was reported to be within $2.6\text{-}3.27\times10^{-9}$ $m^2\cdot s^{-1}$ at 25°C (Jawalkar and Aminabhavi, 2007), 1.1×10^{-9} $m^2\cdot s^{-1}$ at 27°C (Charati and Stern, 1998; Robb, 1968), around 11×10^{-9} $m^2\cdot s^{-1}$ at 28°C (Tremblay et al., 2006), whereas at 35°C D_p has been altered between 2.2×10^{-9} $m^2\cdot s^{-1}$ (Merkel et al., 2000), and 2.6×10^{-9} $m^2\cdot s^{-1}$ (Charati and Stern, 1998; Walker et al., 2002). All these results indicate that D_p is not only very sensitive to the ambient temperature and pressure, but also to the differences in the PDMS because of the different fabrication processes used. Furthermore, some variations between the experimental and simulation values could exist because of the assumptions made in the model (Jawalkar and Aminabhavi, 2007).

Another issue to be discussed is the diffusion coefficient of CO_2 in liquid (water in this work), D_l. Typically, in the literature this value is $1.6\text{-}2.8\times10^{-9}$ $m^2\cdot s^{-1}$ (Farajzadeh et al., 2007; Farajzadeh et al., 2009; Sell et al., 2013; Walker et al., 2002; Xu et al., 2012) at a standard ambient temperature and pressure, thus over one magnitude lower than determined in this work (30×10^{-9} $m^2\cdot s^{-1}$). However, in our case the density-driven natural convection that enhances the mass transport of CO_2 is a possible reason for the higher value of D_l. Natural convection appears when concentration and density gradients are generated by CO_2 dissolved into water. The generated density gradient results in a remarkably faster mass transport than expected from pure Fickian diffusion (Farajzadeh et al., 2007; Farajzadeh et al., 2009, Lindeberg and Wessel-Berg, 1997). In our work, this natural convection enhanced mass transport has been taken into account by replacing the known diffusion coefficient of CO_2 in water as a larger effective diffusion coefficient value. However, natural convection could be better modeled by using two different effective diffusion coefficients values as proposed by Farajzadeh *et al.* (Farajzadeh et al., 2007). They used one coefficient value in the beginning of transport process when density driven natural convection is more important, and another smaller coefficient in later stages. In their device, 43.5×10^{-9} $m^2\cdot s^{-1}$ was used for D_l in the early stages at 7.72 bar initial pressure, and they claimed that this value should be increased when pressure is increased. Using linear fitting based on their experimental data in three different pressures, 7.72-20.10 bar (Farajzadeh et al., 2007), approximated D_l at the early

stage at atmospheric pressure is around 20×10^{-9} $m^2 \cdot s^{-1}$, and is similar to value determined in this work. Therefore, we believe that natural convection should be considered in the devices covered in this paper.

5.2. Model validation using pH measurements

This section reports validation of the computational model (presented in Section 3.1) using a complete device and pH experiments (as described in Section 3.2). A time-dependent 2D simulation was used to describe CO_2 transport and concentration distribution in the device. One simulation result showing concentration distribution in liquid phase is illustrated in Fig. 7.

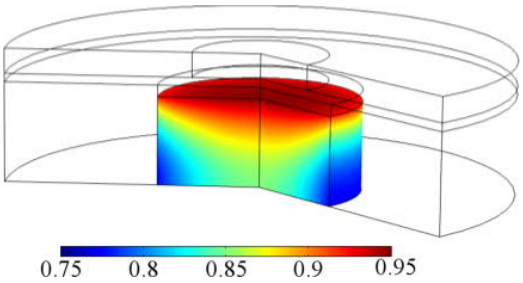

Fig. 7. Simulated CO_2 concentration [mol/dm^3] in liquid phase at time 500min.

To compare the simulated results to the pH measurement, an average volume concentration from the simulation is converted to pH using Eq. (10). Simulation results are compared to measured data in Fig. 8.

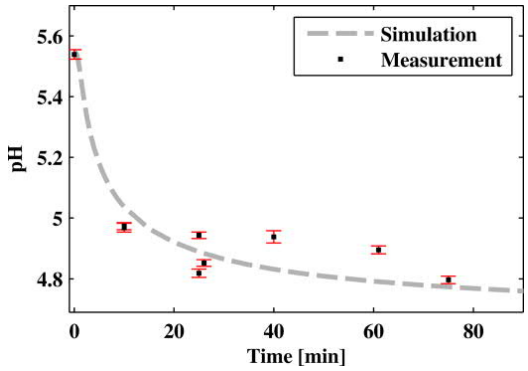

Fig. 8. pH measurement: Simulated versus experimental pH. Each measurement point represents an average pH and a standard deviation value of continuous two minutes recording as described in Section 3.2.

As illustrated in Fig. 8, the developed model predicts remarkably well the dynamics of the experimental pH values. When comparing simulation and measurement data from the first 75 minutes, only maximum 0.1 pH difference is obtained. Furthermore, the simulated saturation value (pH = 4.72) is close to four measured values (pH = 4.73-4.85) obtained in the long-term experiments as reported in Section 3.2. It should be remember that, as stated in Section 3.2,

in the experiments pH was measured by removing the connection cap and taking a 200 µl sample, causing some variations to the measured pH values. Nevertheless, the results indicate that the developed model is able to estimate the CO_2 transportation also in a complete device.

An important issue to point out is that in this study, pH measurements were performed in water without cells or cell culture medium. It is expected, that the results with cell culture medium would differ compared to results presented in this paper because pH of culture medium is usually buffered such that the pH level is approximately 7.4 when 5% CO_2 is present. Therefore, Eq. (10) could not be used to calculate liquid pH. However, we expect that the transport of CO_2 molecules through the device is not significantly changed if water is changed to cell culture medium.

5.3. Simulation case study

The aim of the case study is to demonstrate how the developed model is used as a designing tool. In the selected simulation study, we used a time-dependent model to investigate how CO_2 is transported to the bottom of the chamber with different set-ups. The purpose here is not to fully optimize the structure, but only to demonstrate how simple geometry and set-up modifications can change the system response.

First, the model is changed to study effects of different CO_2 concentrations in the device performance. A schematic of the device was shown in Fig. 2, and the model used was presented in Fig. 4, except that now different feeding CO_2 concentrations (5-20%) were set to the top gas layer. Chamber temperature and pressure were assumed to be 24°C and 1 atm, respectively. Initially, all the phases were assumed to be saturated to air concentration (~0.04% CO_2). Average CO_2 concentrations in the bottom of the chamber with different feeding CO_2 concentrations are presented in Fig. 9. Simulation shows that when 5% CO_2 is set to the upper gas boundary, less than 2.3% CO_2 concentration is transported to the bottom of the chamber in the first ten hours. This is not desired in cell applications, as the lack of CO_2 in cell medium results in an increase in pH. Thus, this would prevent long-term cell culturing in these types of devices (Forry and Locascio, 2011). Therefore, we investigated the required level to achieve 5% CO_2 in the bottom of the chamber by increasing the feeding CO_2 concentration from 5% up to 20%. Results indicate that by using 10% CO_2 feeding concentration, CO_2 concentration in the bottom of the chamber is approximately 4.5%, thus over 10% CO_2 feeding concentration is required to achieve the desired 5% CO_2 level.

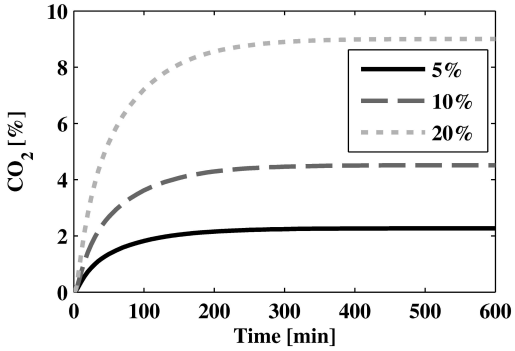

Fig. 9. Simulated average CO_2 concentration (in %) in the bottom of the chamber with different feeding concentrations.

In the model, CO_2 concentration at the outer boundaries was set to 0.04%, representing a typical amount of CO_2 in air. Next, we studied a case where the device is placed inside a conventional incubator where 5% CO_2 concentration is surrounding the device. This is modeled by changing concentration on the outer boundaries (marked as Air Concentration in Fig. 4) from 0.04% to 5%. As expected, the device performance was changed. Results from the two simulations are compared in Fig. 10. It shows how bringing CO_2 not only from the top, guarantees the desired concentration.

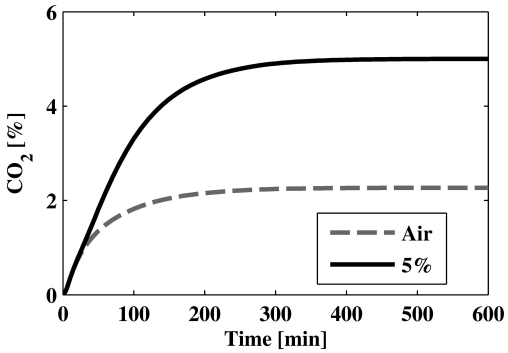

Fig. 10. Simulated average CO_2 amount (in %) in the bottom of the chamber when the CO_2 concentration at outer boundaries are set to air concentration (0.04%) and 5%.

Based on the results presented in Fig. 10, using 5% concentration at outer boundaries, over seven hours is required to achieve 5% CO_2 concentration in the bottom of the chamber. It is clear, that significantly faster response would be desirable. Therefore, we used our model to study how the diameter of the outer PDMS ring (originally 30 mm as shown in Fig. 2) affects the CO_2 transport. The results with three different outer diameters are plotted in Fig. 11.

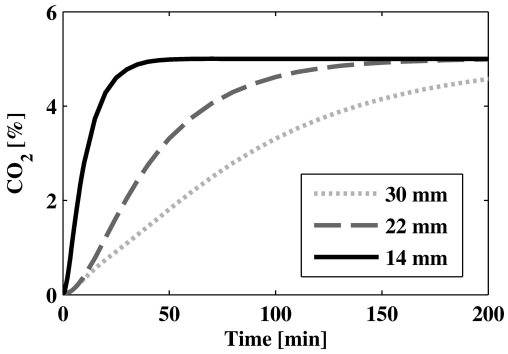

Fig. 11. Simulated average CO_2 amount (in %) in the bottom of the chamber with three different outer PDMS ring diameters. Outer boundaries are set to 5% CO_2.

Based on simulation results given in Fig. 11, the required time to achieve the desired 5% CO_2 concentration in the bottom of chamber is reduced from over seven hours with 30 mm to only one hour with 14 mm outer diameter, respectively. In addition, device rise time (time taken for the output to reach 90 % of steady state output value) is decreased from over 3h with 30 mm outer diameter ring to less than 25 minutes when using a ring with a 14 mm outer diameter. Therefore, the simulation suggests that it is desirable to design a device where the required CO_2 concentration is brought not only from the top but also around the device. Furthermore, it is possible to achieve a faster system response by using a thinner PDMS membrane between gas and liquid. In addition, this approach can minimize or even eliminate unwanted concentration gradients, thus provide more uniform CO_2 concentration profile in the device.

6. Conclusion

Even though oxygen transport in PDMS-based microfluidic cell culture devices is extensively modeled, to the best of our knowledge, there is no comprehensive model to simulate CO_2 transport in these devices. Therefore, a new numerical model based on finite element method was developed for study CO_2 transport in PDMS-based devices. Firstly, this model was validated using experimental data from several different measurements. The results clearly demonstrated that the model predicted successfully the CO_2 concentration in different devices and geometries. Simulations allowed us for studying multiple different experimental conditions remarkably faster than that actually testing these systems, thus saving time and cost in the designing process. In addition, our aim was to demonstrate how the model and computer simulation provide a useful designing tool for microfluidic cell culture devices. For example, we studied a typical case where CO_2 is fed only from top of the device to control medium pH. Based on the simulation

results, this is not necessary optimal solution for PDMS-based devices because of the gas permeable walls. Therefore, the proposed model can be effectively used to optimize the geometry of the PDMS-based microfluidic cell culture device, to study the device response with different CO_2 input concentrations, and to compare different CO_2 feeding strategies.

Acknowledgments

The authors would like to thank the financial support from the Doctoral Programme of the President of the Tampere University of Technology (TUT) and Tekes, the Finnish Funding Agency for Technology and Innovation (Decision Nos. 40346/11). The work was carried out within the Human Spare Parts project.

Nomenclature

A	parameter *A* used in Eq. (11) for H_2CO_3
B	parameter *B* used in Eq. (11) for H_2CO_3
c	molar concentration, $mol \cdot m^{-3}$
C	parameter *C* used in Eq. (11) for H_2CO_3
D	diffusion coefficient, $m^2 \cdot s^{-1}$
F	volume force, $N \cdot m^{-3}$
Flux	flux, $mol \cdot (s \cdot m^3)^{-1}$
Fv	volume fraction
H	constant used to calculate *kh*, K
k	mass transport coefficient, $m \cdot s^{-1}$
Kc	thermodynamic constant for the dissociation of $[H_2CO_3]$
kh	Henry's law constant, $l \cdot atm \cdot mol^{-1}$
Khyd	dissociation constant of H_2CO_3 in water
Kp	partition coefficient ratio
Kw	ion product of water
M1	measurement set 1
M2	measurement set 2
n	amount of substance, mol

$\boldsymbol{N}$	arbitrary flux expression, $mol\cdot(s\cdot m^2)^{-1}$
np	pressure difference of solubility, atm^{-1}
p	pressure, Pa
P	permeability coefficient, $cm^3(STP)\cdot cm\cdot(cm^2\cdot s\cdot atm)^{-1}$
R	universal gas constant, $8.31451 J\cdot(K\cdot mol)^{-1}$
S	solubility, $cm^3(STP)\cdot(cm^3\cdot atm)^{-1}$
SD	standard deviation
Sinf	infinite dilution solubility, $cm^3(STP)\cdot(cm^3\cdot atm)^{-1}$
T	temperature, K
$\boldsymbol{u}$	velocity field, $m\cdot s^{-1}$
V	volume, m^3

Greek letters

ρ	fluid density, $kg\cdot m^{-3}$
η	fluid dynamic viscosity, Pa·s

Subscripts

_sat	saturated (concentration)
ch	chamber (pressure)
CO2	carbon dioxide (partial pressure or volume fraction)
g	gas-phase
gl	gas-liquid
gp	gas-PDMS
H(T)	Henry's law constant at experiment temperature *T*
H0	Henry's law constant at standard ambient temperature
l	liquid-phase
lg	liquid-gas
lp	liquid-PDMS
p	solid-phase (PDMS)
pg	PDMS-gas

pl	PDMS-liquid
SATP	standard ambient temperature (298.15 K)

References

Adler, M., Polinkovsky, M., Gutierrez, E., Groisman, A., 2010. Generation of oxygen gradients with arbitrary shapes in a microfluidic device. Lab on a Chip - Miniaturisation for Chemistry and Biology 10(3), 388-391.

Blau, A., Neumann, T., Ziegler, C., Benfenati, F., 2009. Replica-moulded polydimethylsiloxane culture vessel lids attenuate osmotic drift in long-term cell cultures. Journal of Biosciences 34(1), 59-69.

Charati, S. G., Stern, S. A., 1998. Diffusion of gases in silicone polymers: Molecular dynamics simulations. Macromolecules 31(16), 5529-5535.

Chen, Y. - A., King, A. D., Shih, H. - C., Peng, C. - C., Wu, C. - Y., Liao, W. - H., Tung, Y. - C., 2011. Generation of oxygen gradients in microfluidic devices for cell culture using spatially confined chemical reactions. Lab on a Chip - Miniaturisation for Chemistry and Biology 11(21), 3626-3633.

Clark, W. M., Jackson, Y. Z., Morin, M. T., Ferraro, G. P., 2011. Combining experiments and simulation of gas absorption for teaching mass transfer fundamentals: Removing CO2 from air using water and NaOH. Chemical Engineering Education 45(2), 133-143.

Davidson, E. A., Trumbore, S. E., 1995. Gas diffusivity and production of CO2 in deep soils of the eastern Amazon, Tellus, Series B 47 B(5), 550-565.

Duffy, D. C., McDonald, J. C., Schueller, O. J. A., Whitesides, G. M., 1998. Rapid prototyping of microfluidic systems in poly(dimethylsiloxane). Analytical Chemistry 70(23), 4974-4984.

Farajzadeh, R., Barati, A., Delil, H. A., Bruining, J., Zitha, P. L. J., 2007. Mass transfer of CO2 into water and surfactant solutions. Petroleum Science and Technology 25(12), 1493-1511.

Farajzadeh, R., Zitha, P. L. J., Bruining, J., 2009. Enhanced mass transfer of CO2 into water: Experiment and modeling. Industrial and Engineering Chemistry Research 48(13), 6423-6431.

Forry, S. P., Locascio, L. E., 2011. On-chip CO 2 control for microfluidic cell culture. Lab on a Chip - Miniaturisation for Chemistry and Biology 11(23), 4041-4046.

Gao, Y., Sun, J., Lin, W. - H., Webb, D. J., Li, D., 2012. A compact microfluidic gradient generator using passive pumping. Microfluidics and Nanofluidics 12(6), 887-895.

Han, J., Eimer, D. A., Melaaen, M. C., 2013. Liquid phase mass transfer coefficient of carbon dioxide absorption by water droplet, Energy Procedia 37, 1728-1735.

Inamdar, N. K., Griffith, L. G., Borenstein, J. T., 2011. Transport and shear in a microfluidic membrane bilayer device for cell culture. Biomicrofluidics 5(2).

Jawalkar, S. S., Aminabhavi, T. M., 2007. Molecular dynamics simulations to compute diffusion coefficients of gases into polydimethylsiloxane and poly{(1,5- naphthalene)-co-[1,4-durene-2,2?-bis(3,4-dicarboxyl phenyl)hexafluoropropane diimide]}. Polymer International 56(7), 928-934.

Kim, L., Toh, Y. - C., Voldman, J., Yu, H., 2007. A practical guide to microfluidic perfusion culture of adherent mammalian cells. Lab on a Chip - Miniaturisation for Chemistry and Biology 7(6), 681-694.

Kuo, A. C. M., 1999. Polymer Data Handbook, Oxford University Press, Oxford, UK.

Lindeberg, E., Wessel-Berg, D., 1997. Vertical convection in an aquifer column under a gas cap of CO2, Energy Conversion and Management 38(SUPPL. 1), S229-S234.

Liu, N., Aymonier, C., Lecoutre, C., Garrabos, Y., Marre, S., 2012. Microfluidic approach for studying CO2 solubility in water and brine using confocal Raman spectroscopy. Chemical Physics Letters 551, 139-143.

Merkel, T. C., Bondar, V. I., Nagai, K., Freeman, B. D., Pinnau, I., 2000. Gas sorption, diffusion, and permeation in poly(dimethylsiloxane). Journal of Polymer Science, Part B: Polymer Physics 38(3), 415-434.

McKeen, L. W., 2012. Permeability Properties of Plastics and Elastomers, third ed. William Andrew Applied Science, Norwich, New York, USA, pp. 309.

Millero, F. J., Pierrot, D., 1998. A chemical equilibrium model for natural waters. Aquatic Geochemistry 4(1), 153-199.

Ocampo-Torres, F. J., Donelan, M. A., 1994. Laboratory measurements of mass transfer of carbon dioxide and water vapour for smooth and rough flow conditions, Tellus, Series B 46 B(1), 16-32.

Polinkovsky, M., Gutierrez, E., Levchenko, A., Groisman, A., 2009. Fine temporal control of the medium gas content and acidity and on-chip generation of series of oxygen concentrations for cell cultures. Lab on a Chip - Miniaturisation for Chemistry and Biology 9(8), 1073-1084.

Robb, W. L., 1968. Thin silicone membranes--their permeation properties and some applications. Annals of the New York Academy of Sciences 146(1), 119-137.

Sander, R., 1999. Compilation of Henry's Law Constants for Inorganic and Organic Species of Potential Importance in Environmental Chemistry (Version 3). Available from http://www.henrys-law.org.

Sell, A., Fadaei, H., Kim, M., Sinton, D., 2013. Measurement of CO2 diffusivity for carbon sequestration: A microfluidic approach for reservoir-specific analysis. Environmental Science and Technology 47(1), 71-78.

Shah, V. M., Hardy, B. J., Stern, S. A., 1993. Solubility of carbon dioxide, methane, and propane in silicone polymers. Effect of polymer backbone chains. Journal of Polymer Science, Part B: Polymer Physics 31(3), 313-317.

Shiku, H., Saito, T., Wu, C. - C., Yasukawa, T., Yokoo, M., Abe, H., Matsue, T., Yamada, H., 2006. Oxygen permeability of surface-modified poly(dimethylsiloxane) characterized by scanning electrochemical microscopy. Chemistry Letters 35(2), 234-235.

Skolimowski, M., Nielsen, M. W., Emnéus, J., Molin, S., Taboryski, R., Sternberg, C., Dufva, M., Geschke, O., 2010. Microfluidic dissolved oxygen gradient generator biochip as a useful tool in bacterial biofilm studies. Lab on a Chip - Miniaturisation for Chemistry and Biology 10(16), 2162-2169.

Stoian, A. V., Druon-Bocquet, S., Groux, H., Sanchez, J., 2012. Modeling and simulation of the mass transfer of volatile compounds in a membrane device for toxicity tests. Chemical Engineering Science 80, 160-172.

Takano, A., Tanaka, M., Futai, N., 2012. On-chip CO2 incubation for pocket-sized microfluidic cell culture. Microfluidics and Nanofluidics 12(6), 907-915.

Tanimura, M., 1993. Handbook of Silicone Materials, Tokyo: Toray Dow Corning Silicone.

Terashima, I., Miyazawa, S. -I., Hanba, Y. T., 2001. Why are sun leaves thicker than shade leaves? - Consideration based on analyses of CO2 diffusion in the leaf, Journal of Plant Research 114(1113), 93-105.

Tremblay, P., Savard, M. M., Vermette, J., Paquin, R., 2006. Gas permeability, diffusivity and solubility of nitrogen, helium, methane, carbon dioxide and formaldehyde in dense polymeric membranes using a new on-line permeation apparatus. Journal of Membrane Science 282(1–2), 245-256.

Walker, G. M., Ozers, M. S., Beebe, D. J., 2002. Insect cell culture in microfluidic channels. Biomedical Microdevices 4(3), 161-166.

Xu, B. - Y., Hu, S. - W., Yan, X. - N., Xia, X. - H., Xu, J. - J., Chen, H. - Y., 2012. On chip steady liquid-gas phase separation for flexible generation of dissolved gas concentration gradient. Lab on a Chip - Miniaturisation for Chemistry and Biology 12(7), 1281-1288.

Zahorodny-Burke, M., Nearingburg, B., Elias, A. L., 2011. Finite element analysis of oxygen transport in microfluidic cell culture devices with varying channel architectures, perfusion rates, and materials. Chemical Engineering Science 66(23), 6244-6253.